SCIENTIFIC REPORTS

OPEN

Core-shell $NaGdF_4$@$CaCO_3$ nanoparticles for enhanced magnetic resonance/ultrasonic dual-modal imaging via tumor acidic micro-enviroment triggering

Received: 29 November 2016
Accepted: 30 May 2017
Published online: 14 July 2017

Zuwu Wei[1,2], Xiao Lin[3], Ming Wu[1,2], Bixing Zhao[1,2], Ruhui Lin[4], Da Zhang[1,2], Yun Zhang[5], Gang Liu[6], Xiaolong Liu[1,2] & Jingfeng Liu[1,2,3]

For cancer diagnosis, a paramount challenge still exists in the exploring of methods that can precisely discriminate tumor tissues from their surrounding healthy tissues with a high target-to-background signal ratio. Here, we report a $NaGdF_4$@$CaCO_3$-PEG core-shell nanoparticle which has the tumor acidic microenvironment enhanced imaging signals of ultrasound and magnetic resonance. Under the acidic conditions, the $CaCO_3$ shell will gradually dissolve which then facilitate the interaction of $NaGdF_4$ with the external aqueous environment to enhance water proton relaxation. Meanwhile, the CO_2 bubbles generated by the $CaCO_3$ dissolvement will generate strong elastic echo for US detection. The core-shell structure of $NaGdF_4$@$CaCO_3$-PEG can be observed by TEM, and its composition can be determined by STEM. The acid triggered generation of CO_2 bubbles and the enhancement of MRI signal could be demonstrated *in vitro*, and the excellent dual-modal magnetic resonance/ultrasonic cancer imaging abilities of $NaGdF_4$@$CaCO_3$-PEG could be also proved at the tumor site *in vivo*. The here described proof-of-concept nanoparticles with pH triggered magnetic resonance/ultrasonic dual-modal imaging enhancement, may serve as a useful guide to develop various molecular imaging strategies for cancer diagnosis in the future.

Cancer is becoming to one of the most dreaded disease and still remains as a major threat to human life[1]. The rising burden is ascribed to population growth, aging and an adoption of cancer-associated lifestyle choices including smoking, physical inactivity, etc[1,2]. Even worse, most patients were diagnosed at a later or advanced stage, which results in poor prognosis[1,3]. Therefore, early diagnosis of cancer is crucial for timely therapy to prevent the potential risk of cancer metastasis and improve the long-term survival. Many non-invasive biomedical imaging techniques have been applied in the diagnosis of cancer including magnetic resonance imaging (MRI)[4–9], ultrasound imaging (US)[10,11], positron emission tomography (PET)[12–15], and computed X-ray tomography (CT)[16–19], etc. Among the clinically applied diagnostic modalities, MRI has a high potential to image the tissue pathological changes, as it could safely provide high spatial resolution information[20]. On the other hand, as a noninvasive real-time imaging modality, US has serveal advantages such as high safety, low cost, and easy accessed by the public. However, the sensitivity of conventional MRI and US strategies heavily rely on contrast agents (CAs), such as

[1]The United Innovation of Mengchao Hepatobiliary Technology Key Laboratory of Fujian Province, Mengchao Hepatobiliary Hospital of Fujian Medical University, Fuzhou, 350025, People's Republic of China. [2]The Liver Center of Fujian Province, Fujian Medical University, Fuzhou, 350025, People's Republic of China. [3]Liver Disease Center, the First Affiliated Hospital of Fujian Medical University, Fuzhou, 350025, People's Republic of China. [4]Academy of Integrative Medicine, Fujian University of Traditional Chinese Medicine, Fuzhou, 350122, People's Republic of China. [5]Key Laboratory of Design and Assembly of Functional Nanostructures, Fujian Institute of Research on the Structure of Matter, Chinese Academy of Sciences, Fuzhou, 350002, People's Republic of China. [6]Center for Molecular Imaging and Translational Medicine, Xiamen University, Xiamen, 361102, People's Republic of China. Zuwu Wei and Xiao Lin contributed equally to this work. Correspondence and requests for materials should be addressed to X.Liu (email: xiaoloong.liu@gmail.com) or J.L. (email: drjingfeng@126.com)

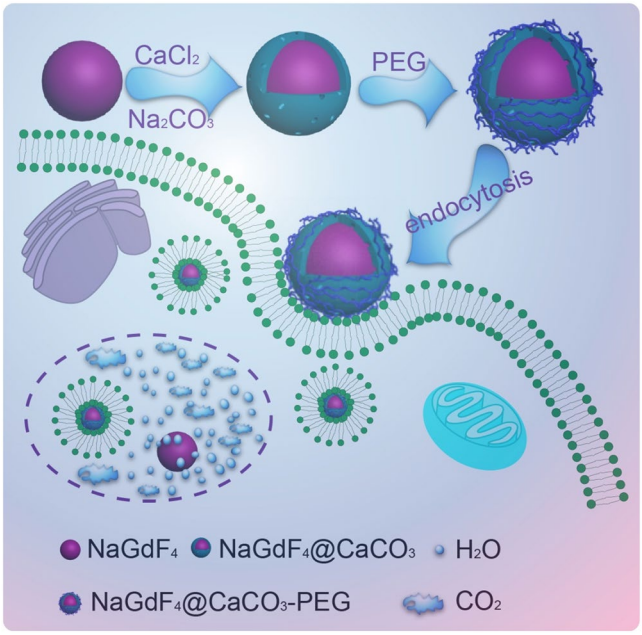

Figure 1. Schematic illustration of the synthesis of $NaGdF_4$@$CaCO_3$-PEG nanoparticle and its bioimaging application.

the widely used paramagnetic gadolinium ions (Gd-(DTPA)]$^{-2}$ (Magnevist) and [Gd-(DOTA)]$^{-1}$ (Dotarem)[21–23], or gas-filled echogenic microbubbles[24,25], that are always "on", emitting constant signals regardless of their proximity or interaction with target tissues, cells, or environmental markers. As a result, a large volume of nonspecific signal which might lead to a poor signal-to-noise ratio, makes the anatomical features of interested tissue difficult to distinguish. A more attractive contrast agent whose signal should be switched from OFF to ON in response to specific biological stimulus, which will further maximize the signals of targets and minimize the background signals, which in turn could improve the sensitivity and specificity[26–29].

Several activatable CAs that respond to tumour-related factors, such as pH and redox potential, have been developed for tumour-specific MRI or US. For example, Mi *et al.* have reported a MRI contrast agent that rapidly amplify the magnetic resonance signals in response to pH via releasing confined Mn^{2+} ions from pH-sensitive calcium phosphate (CaP) nanoparticles to the aqueous environment[30]. Min *et al.* developed the calcium carbonate ($CaCO_3$) nanopartciles which exhibited strong echogenic signals at tumoral acid pH by producing CO_2 bubbles and showed excellent echo persistence[10]. Even so, some intrinsic drawbacks of US and MRI still cannot be avoided, for example, US has a poor tissue discrimination ability while MRI cannot provide real-time images and usually time consuming. Thus, developing a sensitive dual modal imaging (US and MRI) agent would not only make them as favorable tools for precisely visualizing biological and physiological changes with high signal-to-noise ratio, but also would render synergistic efficacy to overcome their own inherent limitations[31].

As a MRI contrast agent, various size of $NaGdF_4$ nanoparticles (NPs) with well-defined size distributions could be readily synthesized via pyrolysis methods[32–35]. Their MRI performances have been demonstrated to increase with the decreasing of the NPs' size, attributed to the increased number of surface Gd^{3+} ions relative to the core ions. Therefore, it will be very useful to synthesize ultrasmall $NaGdF_4$ NPs, e.g., smaller than 5 nm, to provide better MRI signals[6]. Furthermore, compared with the Gd-(DTPA) or Gd-(DOTA), the renal clearable Gd-based NPs would have better biosafty since it could not induce the excessive Gd^{3+} ion leakage to cause biological toxicity[36,37], therefore it might be a more promising candidate for disease diagnosis. As for a new type of US contrast agent, $CaCO_3$ nanoparticles with rigid structure can penetrate into host tumoral environments for cancer imaging, while the frequently used gas-filled microbubbles suffer from inherent drawbacks, such as low stability, short half-life in blood and low penetration ability due to the large size, which is limited to the imaging of intravascular structures.

Herein, we designed a pH-responsive nanoparticle which could significantly enhance the contrast of MRI and US signals in tumor as illustrated in Fig. 1. The shell of $CaCO_3$ was deposited onto the core surface of $NaGdF_4$ nanoparticles through the microemulsion method; in addition, physicochemical properties of nanoscale systems, such as size, dispersibility, and toxicity were systematically analyzed; furthermore, the US and MRI imaging enhanced efficiency were both evaluated *in vitro* and *in vivo*, which clearly proved that our probe could be utilized for sensitive and specific tumor imaging with responding to extracellular acidic microenvironments.

Results and Discussion

Characterization of $NaGdF_4$@$CaCO_3$-PEG. As shown in Fig. 1, monodispersed spherical $NaGdF_4$ nanocrystals were chosen as the morphology-deciding template to obtain magnetic nanoparticles, which were fabricated by thermal decomposition method using rare earth perchlorate as the RE precursor. From TEM images

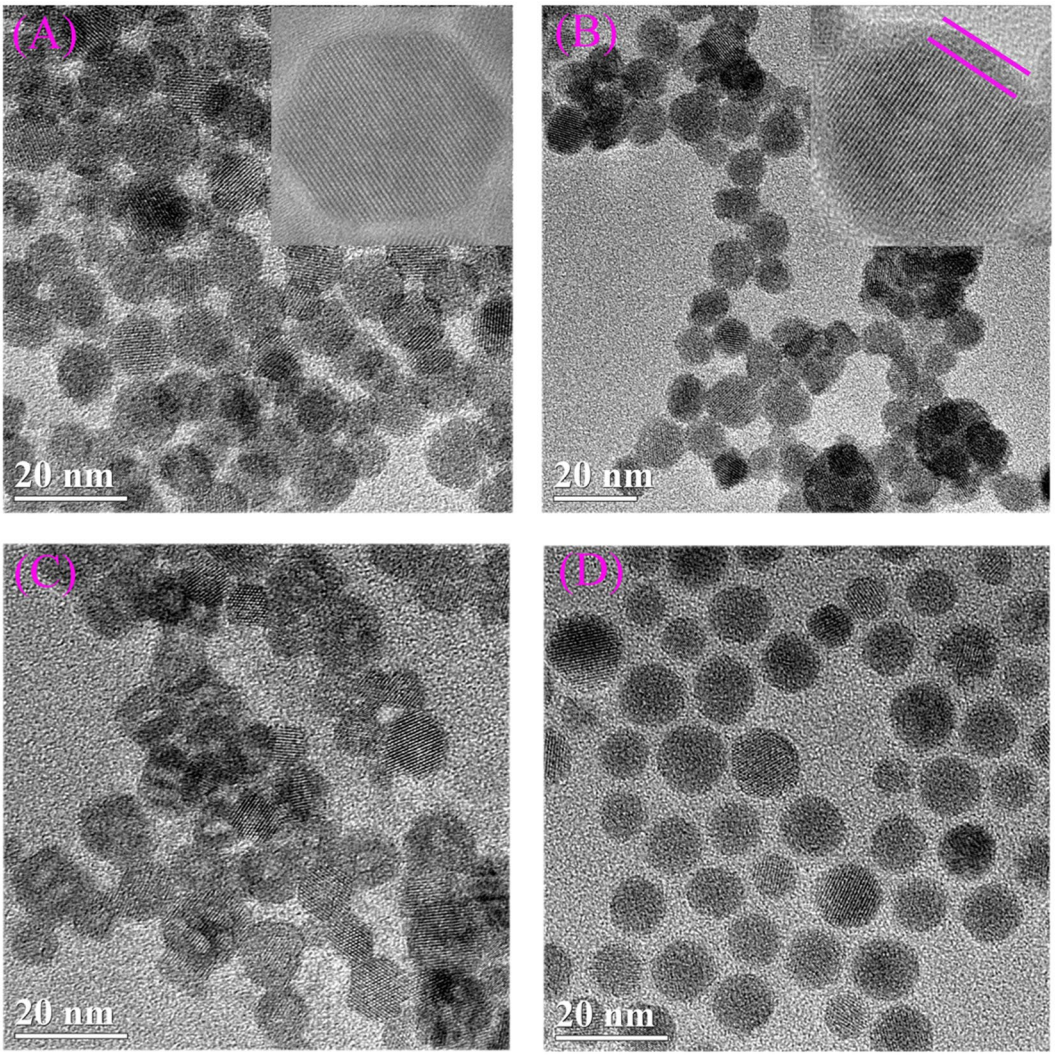

Figure 2. Structural characterization of nanoparticles. $NaGdF_4$ dispersed in cyclohexane (**A**); $NaGdF_4$@$CaCO_3$ (**B**) and $NaGdF_4$@$CaCO_3$-PEG (**C**) dispersed in H_2O; and $NaGdF_4$@$CaCO_3$-PEG dispersed in PBS (pH 5.0).

(Fig. 2A), the synthesized $NaGdF_4$ exhibit a very well particle size distribution around 8~10 nm, with a regular spherical morphology. A thin layer of dense $CaCO_3$ was deposited onto the surface of $NaGdF_4$ to form $NaGdF_4$@$CaCO_3$ core/shell nanoparticles by the well-known microemulsion method, which could further transfer the hydrophobic $NaGdF_4$ nanoparticle into aqueous soltion. In detail, the $CaCl_2$ aqueous solution was first added into the cyclohexane solution of hydrophobic $NaGdF_4$, while triton X-100, 1-hexanol were used as nonionic surfactants to create a stable water-in-oil emulsion after vigorous stirring. At this stage, the hydrophobic $NaGdF_4$ will transfer from oil phase to water droplets as the surfactants can self-assemble on these nanoparticles. Meanwhile, the hydrophilic groups (hydroxyl) of the surfactants has a well affinity with Ca^{2+} which could recruit these ions on the surfaces of the $NaGdF_4$ nanoparticles. After adding Na_2CO_3 aqueous solution, the precipitation reaction between Ca^{2+} and CO_3^{2-} therefore produces a layer of $CaCO_3$ on the $NaGdF_4$ nanoparticles. The obtained nanoparticles show a size of 10~12 nm, as well as with aspherical-like morphology. Then, PEG_{8000} was adsorbed on the surface of $NaGdF_4$@$CaCO_3$ nanoparticles through Van der Waals' force, which could award good water dispersibility. Element mapping of $NaGdF_4$@$CaCO_3$-PEG with a thin or thick shell all shows the co-existence of Gd, F and Ca elements (Figure S1), which exhibit a much higher Ca signal compared to the core only $NaGdF_4$ nanoparticles. However, the Ca signal on the surface of $NaGdF_4$ is very weak on the outlayer of $NaGdF_4$ core due to the very small size of $NaGdF_4$ core (10 nm) and the very thin $CaCO_3$ coating layer (2 nm). Nevertheless, we still ensure that the $CaCO_3$ is on the shell because this layer is amorphous, while the $NaGdF_4$ core is highly crystal with noticeable lattice, as shown in the enlarged image inserted in Fig. 2B. In addition, the average size of the $NaGdF_4$ in cyclohexane was further determined to be 8 ± 2 nm by the DLS experiments (Figure S2), which is consistent with the TEM results. After depositon of $CaCO_3$, the average hydrodynamic size of the $NaGdF_4$@$CaCO_3$ and $NaGdF_4$@$CaCO_3$-PEG in water were increased to 100 ± 10 and 120 ± 15 nm, respectively, which may be due to the formation of a hydration layer on the surface of nanoparticles or the formation of small aggregations.

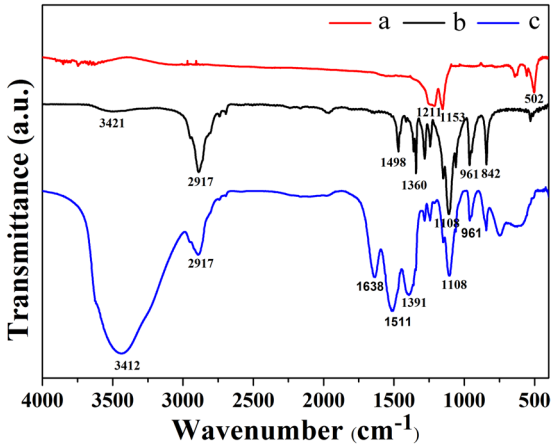

Figure 3. FT-IR spectra of $NaGdF_4$@$CaCO_3$ (a), PEG_{8000} (b) and $NaGdF_4$@$CaCO_3$-PEG (c).

Furthermore, the successful surface PEGlyation of $NaGdF_4$@$CaCO_3$ was also confirmed by FT-IR spectroscopy (Fig. 3). For analyzing the spectrum of PEG_{8000}, the peaks at around 2917 cm^{-1} and 1108 cm^{-1} were observed corresponding to the CH_2 stretching and vibration groups. These two peaks could be also observed in the spectra of $NaGdF_4$@$CaCO_3$-PEG, in addition to the typical peaks of $NaGdF_4$@$CaCO_3$ at 502 cm^{-1}. These results suggest that the PEG_{8000} was successfully modified on the surface of $NaGdF_4$@$CaCO_3$. To make the $CaCO_3$ coating more evident form the IR spectra, we re-fabricated another $NaGdF_4$@$CaCO_3$ with a thicker shell *via* increasing the feeding amount of $CaCl_2$, and analysis their surface groups through FT-IR measurement. The characteristic IR absorption peaks of $CaCO_3$ at 1430, 876, 712 cm^{-1} can be clearly presented in thick layered $NaGdF_4$@$CaCO_3$ (Figure S3).

Before further bio-imaging applications, it is necessary to determine the cytotoxicity of these nanoparticles. To assess the *in vitro* cytotoxicity of $NaGdF_4$@$CaCO_3$-PEG, the standard Cell Counting Kit (CCK-8) assay and live/dead staining were conducted by using LN3 and NIH3T3 cell lines. As shown in Figure S4, cell viability is not affected by the $NaGdF_4$@$CaCO_3$-PEG in the concentration ranged from 0 to 400 $\mu g \cdot mL^{-1}$, which suggested that the $NaGdF_4$@$CaCO_3$-PEG has low cytotoxicity so that it could be further applied for bio-imaging.

***In Vitro* Ultrasound Contrast Enhancement Ability of $NaGdF_4$@$CaCO_3$-PEG.** First, the characteristics of CO_2 gas generation by $NaGdF_4$@$CaCO_3$-PEG was studied through detecting the bubble generation from the particles in PBS buffer with different pH values (pH 7.4, 7.0, 6.8 and 5.0). As shown in Fig. 4, initially, $NaGdF_4$@$CaCO_3$-PEG nanoparticles generate few bubbles at pH 7.4, 7.0 and 6.8, but significantly more bubble generation could be observed at pH 5.0. The degree of bubble generation continuously decreased at pH 5.0 over time, but the bubble generation was first increased and then decreased at pH 7.4, 7.0 and 6.8. The number of bubbles in pH 5.0 was counted to *ca.* 119, which was much higher than that in pH 7.4 (almost no bubbles), after 1 min incubation. However, with increasing the time, the number of bubbles was dramatically decreased at pH 5.0, and only 2 bubbles could be observed after 60 mins incubation (Figure S5). It is noteworthy that bubble generation at lower pH was higher than that at slightly stronger pH at all-time points. This result suggested that the $NaGdF_4$@$CaCO_3$-PEG might enhance US signal in the low pH environment by gas generation, since $CaCO_3$ could generate more CO_2 gas in an acidic environment by improved dissolution, which would be beneficial for imaging the tumor due to a little acidic microenvironment of the tumor micro-environment.

Next, we measured the *in vitro* echogenic performance of the $NaGdF_4$@$CaCO_3$-PEG as a function of pH using an aqueous dispersion test at 37 °C. As shown in Fig. 5, the $NaGdF_4$@$CaCO_3$-PEG at pH 7.4 showed no significant contrast signals under a US field, most likely because the $NaGdF_4$@$CaCO_3$-PEG did not release sufficient CO_2 bubbles for echogenic reflection. This result is well consistent with the results of the pH-dependent CO_2 generation (Fig. 4). In contrast, US contrast images from the $NaGdF_4$@$CaCO_3$-PEG showed first increased and then decreased signal at all-time points at weakly acidic pH conditions (pH 7.0 and 6.8). This is a well understood phenomenon in which the enhanced echo intensity at weakly pH levels is ascribed to the relaxedly facilitated formation of CO_2 bubbles. Due to faster dissolution of $CaCO_3$ phases at pH 5.0, the echo improved immediately and faded away earlier than at higher pH. The excellent echo persistence at weak acidic pH can be ascribed to the relaxedly ionization of $CaCO_3$ solid phases. The contrast enhancement that derives from the $NaGdF_4$@$CaCO_3$-PEG at lower pH suggested that generation of CO_2 bubbles was responsible for echogenic US resonation. US imaging results were further quantitatively analyzed using region-of-interest (ROI) gray value quantification (Figure S6A). The gray value in pH 5.0 and pH 7.4 was respectively determined to be 139.2 ± 10.7 and 14.2 ± 1.2, after 30 min incubation. This result is in accordance with the CO_2 bubbles generation. Meanwhile, in order to further confirm that the US signal was derived from the dissolution of $CaCO_3$ at acidic solution rather than the $NaGdF_4$ itself, we tested US signal of the core-only ($NaGdF_4$) nanoparticle at pH 5.0 and 7.4, and the results are shown in Figure S7. $NaGdF_4$ nanoparticle showed no US signal at both pH 5.0 and 7.4, due to no CO_2 gas generation from $NaGdF_4$ nanoparticle. The feature of gas-generating at a broad range of weak acidic pH would be propitious to US imaging of tumors, which have tissue heterogeneity and diverse acidic pH levels.

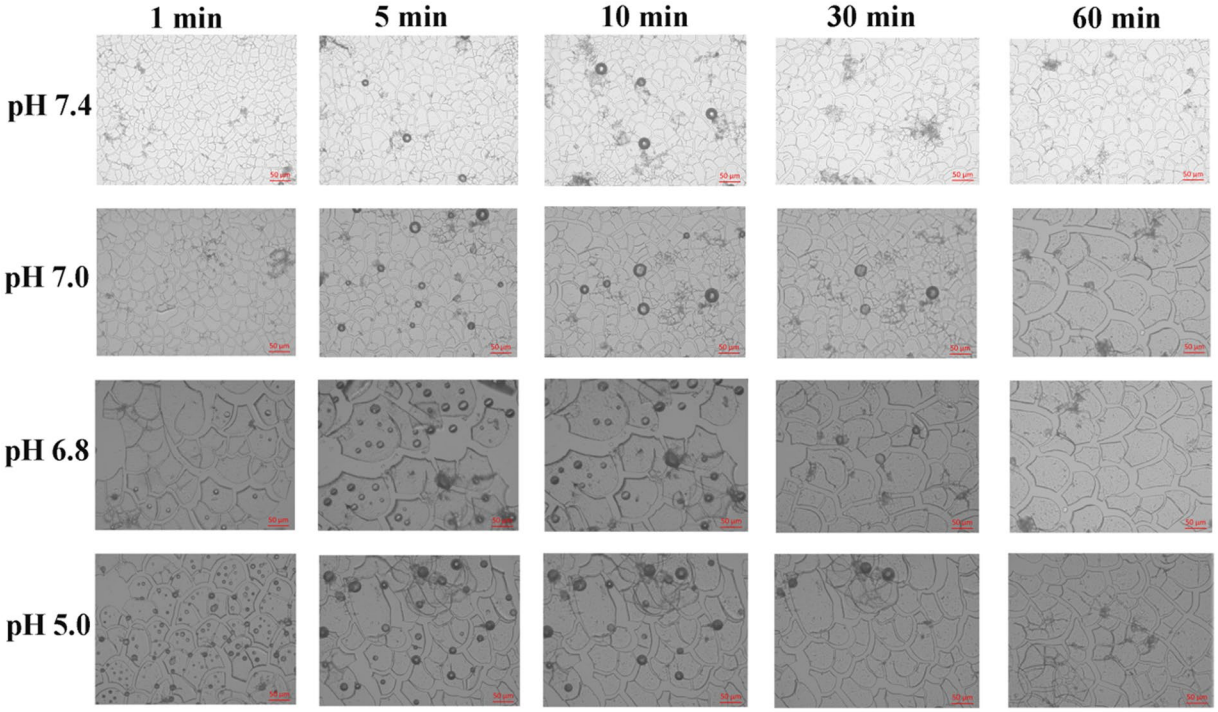

Figure 4. Optical micrographs of CO_2-generation profiles of $NaGdF_4$@$CaCO_3$-PEG incubated in PBS at different pH conditions (pH 5.0, pH 6.8, pH 7.0 and pH 7.4) for 60 min.

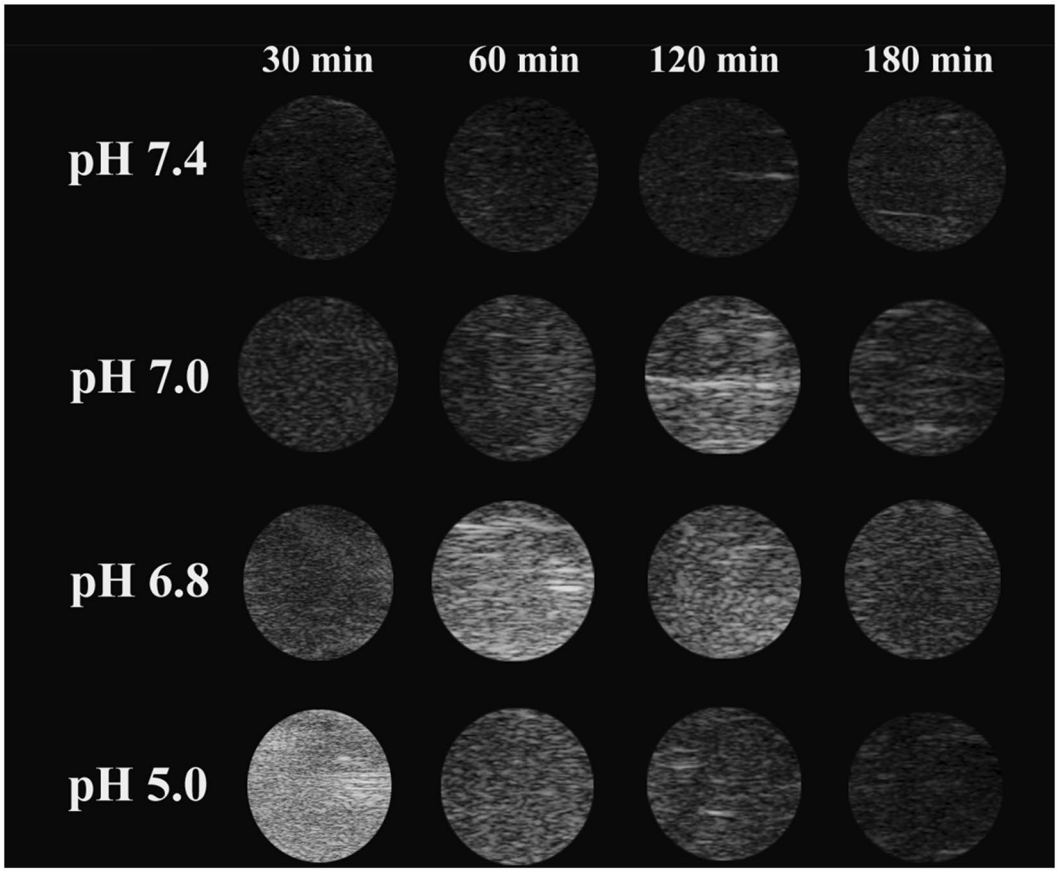

Figure 5. *In vitro* US images from $NaGdF_4$@$CaCO_3$-PEG at various pH (pH 5.0, pH 6.8, pH 7.0 and pH 7.4) conditions along with time.

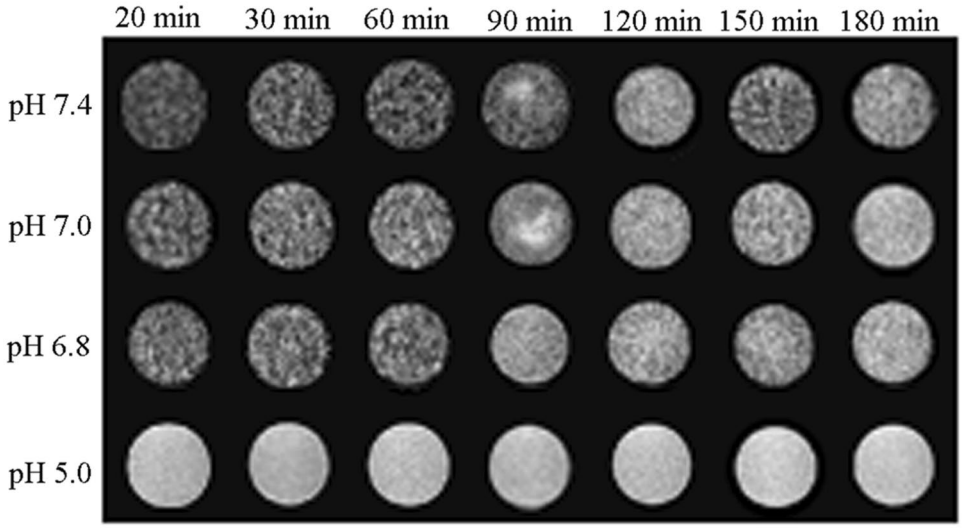

Figure 6. *In vitro* MR images from $NaGdF_4$@$CaCO_3$-PEG at various pH (5.0, 6.8, 7.0 and 7.4) conditions along with the time.

pH-Dependent *In Vitro* MRI Properties of $NaGdF_4$@CaCO3-PEG. Since the doping of Gd^{3+}-ions, $NaGdF_4$@$CaCO_3$-PEG could act as a T_1 MRI contrast agent as well. T_1-weighted MR images of the $NaGdF_4$@$CaCO_3$-PEG showed enhancing signal intensity when Gd^{3+} concentrations were increased. Firstly, the T_1-weighted MR image of the $NaGdF_4$@$CaCO_3$-PEG was studied at different pH conditions. As shown in Fig. 6, the $NaGdF_4$@$CaCO_3$-PEG at pH 7.4 showed no significant enhanced contrast signals under a MRI field, most likely because the shell of $CaCO_3$ did not decompose so that water molecular could not access to $NaGdF_4$ core. In contrast, MRI contrast images from the $NaGdF_4$@$CaCO_3$-PEG were slightly enhanced at weakly acidic pH conditions (pH 7.0, 6.8). It is noteworthy that we demonstrated strongest MRI contrast images at pH 5.0, which might due to the decomposition of the $CaCO_3$ shell so that water molecular could access to the $NaGdF_4$ core. To further demonstrate this mechanism, we compared the T_1-MRI of $NaGdF_4$@$CaCO_3$-PEG to that of core-only ($NaGdF_4$) nanoparticles at pH 7.4, and the results are shown in Figure S6. Of course, $NaGdF_4$ showed a much brighter MR image than $NaGdF_4$@$CaCO_3$-PEG at pH 7.4. With the increasing of incubation time, the contrast of MRI images gradually enhanced at pH 7.2 and 6.8, but almost no change at pH 7.4. MRI imaging results were then quantitatively analyzed using region-of-interest (ROI) gray value quantification (Figure S6B). The gray value in pH 5.0 and pH 7.4 was respectively determined to be 182.2 ± 10.1 and 79.9 ± 3.1, after 20 min incubation. These data are very consistent with the theory that the contrast of T_1 MRI imaging is closely related with water accessibility, and the enhancement of contrast associated with sufficient water contacting.

In addition, the T_1 value of the $NaGdF_4$@$CaCO_3$-PEG was evaluated by using a 0.5 T MRI scanner to determine whether the pH can influence the T_1-weighted MR imaging performance (Fig. 7). As shown in Fig. 7A, the longitudinal (T_1) were measured at 0.5 T magnetic field based on the Gd concentration of $NaGdF_4$@$CaCO_3$-PEG at pH 7.4 and 5.0, and the relaxivities were determined to be 0.42 $mM^{-1} \cdot s^{-1}$ and 1.64 $mM^{-1} \cdot s^{-1}$, respectively. At pH 5.0, it showed about 4 folds higher relaxivity than that at pH 7.4, which further proofed that the T_1-weighted MR imaging enhancement of the $NaGdF_4$@$CaCO_3$-PEG was influenced by pH levels. At the same time, Fig. 7B shows the magnetic resonance signal enhancing capability of the $NaGdF_4$@$CaCO_3$-PEG nanoparticles as a function of Gd concentration ranging from 1.25 to 12.5 mM. Compared with water (Gd, 0 mM), the measured T_1-weighted image contrast gradually increased with the increasing of Gd concentrations.

***In Vivo* US Imaging of Tumor with $NaGdF_4$@CaCO3-PEG.** To verify the potential of $NaGdF_4$@$CaCO_3$-PEG for US imaging of tumor, we executed an intra-tumor injection of $NaGdF_4$@$CaCO_3$-PEG dispersion into LN3 tumor-xenograft-bearing nude mice and monitored the US images as a function of time (Fig. 8). After injection right away, we couldn't acquire any contrast enhancment of the US signal. It is gratifying that enhancement of US signals was obtained after 1 h of injection, and this contrast enhancement maintained more than 2 h. In addition, this phenomenon is very consistent with the *in vitro* experiments. US imaging results were then quantitatively analyzed using region-of-interest (ROI) gray value quantification. As shown in Fig. 8B, the gray value of tumor site was increased from 32.5 ± 3.9 (0 h post-injection) to 53.1 ± 7.8 (1 h post-injection), and still maintained at 38.7 ± 1.35 after 2 h injection. Therefore, we can conclude that the $NaGdF_4$@$CaCO_3$-PEG could generate bubbles in tumor tissues then produce sufficient echogenic reflectivity under a US field.

***In Vivo* MR Imaging of Tumor with using $NaGdF_4$@$CaCO_3$-PEG.** $NaGdF_4$@$CaCO_3$-PEG nanoparticles which have the advantages of highly efficient of T_1 contrast enhancement ability may hold great promise to serve as a novel MRI contrast enhancing agent. Therefore, we performed MRI study on tumor-xenograft-bearing nude mice at a 7.0 T clinical scanner by intratumor injection of $NaGdF_4$@$CaCO_3$-PEG with a dose of 200 μL of 2 $mg \cdot mL^{-1}$. Right after the injection, the MRI contrast enhancement was not found at tumor site; however, after one hour of intratumor injection, we were delighted to find contrast enhancement of MRI signal and the signal

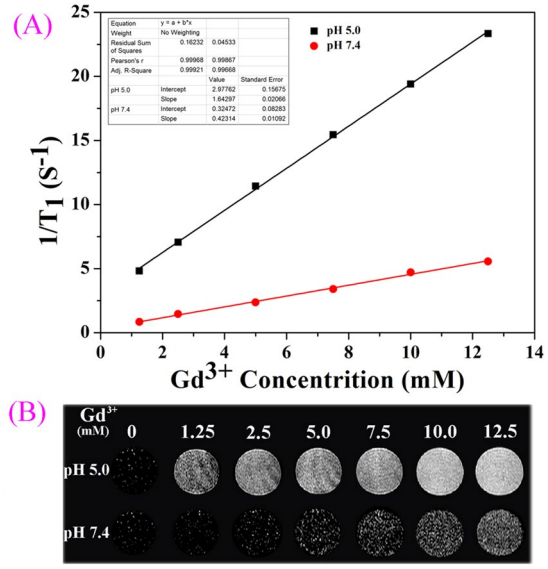

Figure 7. T_1-Weighted MR images of various Gd^{3+} concentrations of $NaGdF_4$@$CaCO_3$-PEG (**A**); relaxation rate r_1 ($1/T_1$) against different Gd^{3+} concentrations of $NaGdF_4$@$CaCO_3$-PEG (**B**).

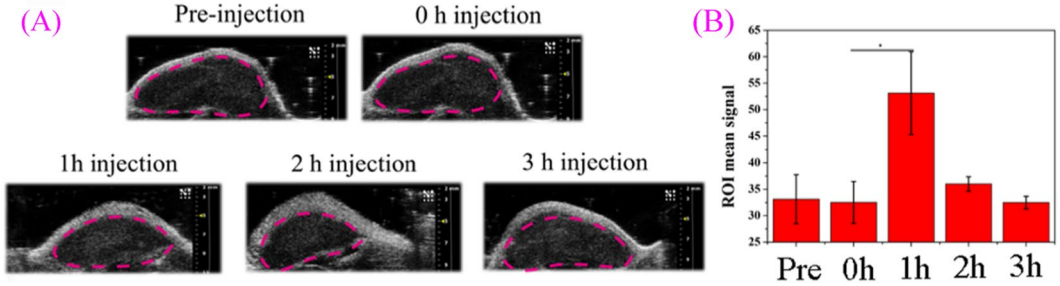

Figure 8. *In vivo* US imaging of the LN3 tumor (red dashed circles) by intratumoral injection of $NaGdF_4$@$CaCO_3$-PEG (**A**); the gray values of mice tumor (region of interest as indicated in **A**), p values were calculated using GraphPad Prism 6 (*$p < 0.05$, **$p < 0.01$, ***$p < 0.001$; $n = 3$).

strength remained unchanged over time up to 3 h (Fig. 9A). T_1 imaging results were then quantitatively analyzed using region-of-interest (ROI) quantification. As shown in Fig. 9B, the gray value of tumor site was increased from 102 (0 h post-injection) to 153 (3 h post-injection). Overall, these results suggested that the $NaGdF_4$@$CaCO_3$-PEG could act as a potential MRI contrast enhancing agent for tumor imaging.

Conclusions

In this work, a core-shell nanoparticle of $NaGdF_4$@$CaCO_3$-PEG was designed as an activatable MR/US dual-modal imaging contrast for cancer diagnosis, which is triggered by the acidic environment. The general idea behind this OFF/ON responsive MR imaging behavior consists of quenching the sphere Gd^{3+} relaxation effects by coating $NaGdF_4$ with a layer of hydrophobic $CaCO_3$ to limit water availability. At acidic aqueous solution, $CaCO_3$ was dissolved to generate CO_2 bubbles which is used to obtain US signal. Meanwhile, a strong MRI enhancement can be activated upon dissolution of $CaCO_3$ and release of the previously silenced $NaGdF_4$ into the aqueous solution. *In vivo* results demonstrated the strong dual-modal magnetic resonance/ultrasonic imaging abilities of $NaGdF_4$@$CaCO_3$-PEG at the tumor site with an acidic environment. We expect that this work may provide a new insight for strategies to design nanomaterials with responsive dual-modal imaging abilities.

Methods

Materials. $Gd(CH_3CO_2)_3$ and PEG_{8000} were purchased from Sigma Aldrich Co., Ltd. Acetone and cyclohexane were obtained from Sinopharm Chemical Reagent Co., Ltd. 1-Octadecene and Methanol was purchased from Alladin Company. Oleic acid was purchased from Alfa Aesar. Cell Counting Kit (CCK-8) was obtained from Dojindo laboratories. Penicillin-streptomycin, fetal bovine serum (FBS), and Dulbecco's Modified Eagle Medium (DMEM) were purchased from Gibco BRL. All of these materials were used as received without further purification. Ultrapure water was used throughout.

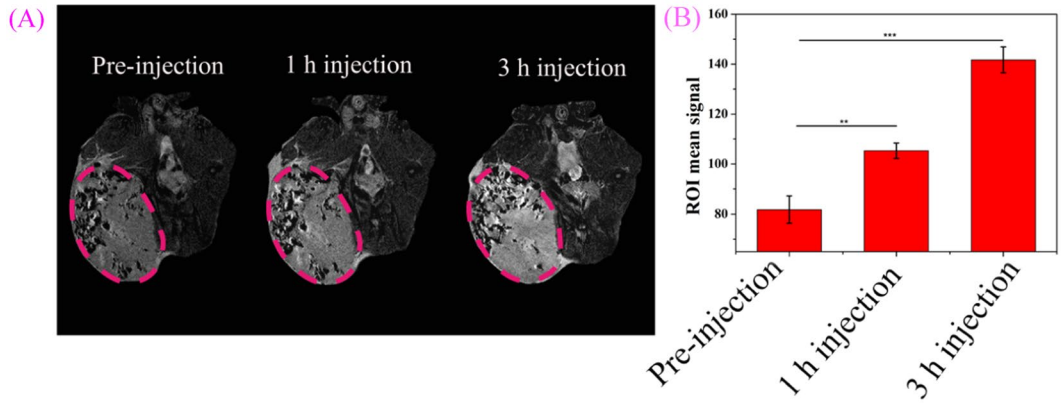

Figure 9. *In vivo* MR imaging of the LN3 tumor (red dashed circles) by intratumoral injection of $NaGdF_4$@$CaCO_3$-PEG (**A**); the gray values of mice tumor (region of interest as indicated in **A**), p values were calculated using GraphPad Prism 6 (*$p < 0.05$, **$p < 0.01$, ***$p < 0.001$; $n = 3$).

Synthesis of $NaGdF_4$ nanoparticles. The synthesis of $NaGdF_4$ nanoparticles is similar to a previous publication about rare-earth up-conversion nanoparticles[34,38]. In brief, 24 mL of $Gd(CH_3CO_2)_3$ (0.2 M) was added to a 500 mL of two-necked round-bottomed flask containing 36 mL of oleic acid. When the mixture was heated to 150 °C for 30 min, 84 mL of 1-octadecene was added and then heated to 150 °C to form the Gd-oleate precursor solution. Then, the reaction system was cooled down to 60 °C naturally and a mixture of 8 mL NaOH (1 M) and 16 mL NH_4F (0.4 M) in methanol was added and stirred for 30 min. The resultant solution was heated at 110 °C for 30 min to remove the methanol, oxygen and water under argon atmosphere. Thereafter, the solution was heated to 300 °C and kept for 1.5 h before cooling down to room temperature. The as-prepared nanoparticles were precipitated by additional of ethanol, collected by centrifugation at 6000 rpm for 3 min, and washed with ethanol for several times. The $NaGdF_4$ nanoparticles are re-dispersed in 50 mL of cyclohexane for further application.

Synthesis of the core-shell $NaGdF_4$@$CaCO_3$-PEG nanoparticles. The core-shell $NaGdF_4$@$CaCO_3$ nanoparticles were prepared through a facile microemulsion method with using $NaGdF_4$ nanoparticles as templates[39]. Briefly, 5 mL $NaGdF_4$ nanoparticles, 10 mL cyclohexane, 3.45 mL Triton X-100, and 3.2 mL 1-hexanol were added to a flask and mixed thoroughly, followed by the addition of a 30 mM solution of calcium chloride (800 μL) to form a well-dispersed water-in-oil emulsion. Then, the solution of sodium carbonate (40 μL, 2.92 M) was added. After keeping moderate stirring for 8 h of the mixture, the as-prepared $NaGdF_4$@$CaCO_3$ nanoparticles were collected by centrifugation and then re-dispersed in 10 mL of ultrapure water. Thereafter, 2 mL PEG_{8000} (0.2 M) aqueous solution was added and stirred for another 8 h, then the as-prepared nanoparticles were collected by centrifugation at 10000 rpm for 15 min, and re-dispersed in 20 mL of ultrapure water for further application.

Characterization of the $NaGdF_4$@$CaCO_3$-PEG nanoparticles. The morphology and the size of the obtained $NaGdF_4$@$CaCO_3$-PEG nanoparticles were performed on a Tecnai F20 transmission electron microscope (TEM, FEI Company, Hillsboro, OR) with an accelerating voltage of 200 kV[40]. For the TEM experiment, the suspension of nanoparticles was dropped onto a carbon-coated copper grid, followed by drying naturally. Scanning transmission electron microscopy (STEM) was obtained using a JEM-2010 electron microscope (JEOL, Japan) to characterize the chemical composition of $NaGdF_4$@$CaCO_3$-PEG nanoparticles[40]. Dynamic light scattering (DLS) experiments were recorded at 25 °C on a NanoZS (Malvern Instruments, UK) with a detection angle of 173°, and a 3 mW He–Ne laser operating at a wavelength of 633 nm. FT-IR spectra were performed on a Fourier transform infrared spectrometer (Perkin-Elmer, Spectrum-2000) over the spectral region of 4000 cm^{-1} to 400 cm^{-1} [41].

Statistical analysis. All quantitative data were expressed as the mean ± standard deviation (SD). Graph Pad Prism version 6.0 was used for statistics analysis. Statistical analysis among different groups was performed using student T-Test. The $P < 0.05$ was considered as statistically significant.

Animals. All mice (4–5 weeks old; weighing: 18–22 g) were obtained from the Center for Animal Experiment of Fujian Medical University (License No: SCXKmin2012–0002), and housed at constant temperature (22 ± 2 °C) and 60% relative humidity, with a light/dark (hours) cycles of 12/12. All animal procedures were conducted in accordance with the approved guidelines of Animal Ethics Committee of Fujian Medical University.

Cytotoxicity assay. The LN3 and NIH3T3 were cultured in Dulbecco's Modified Eagle Medium (DMEM) containing 10% fetal bovine serum and 1% penicillin streptomycin at 37 °C in a humidified atmosphere (5% CO_2). The *in vitro* cytotoxicity was investigated by the Cell Counting Kit (cck-8) assay. In detail, LN3 and NIH3T3 cells were cultured in a 96-well cell-culture plate at a density of 10^4 (100 μL) cells per well for 24 or 48 h, respectively. Then, the medium was replaced with 100 μL fresh medium containing various concentrations of NPs. After 24 or 48 h incubation, the medium was removed. Then, 100 μL of fresh medium and 10 μL of CCK-8 were added and incubated for another 2 h. The absorbance was measured by a Bio-Rad Model-680 microplate reader

at the wavelength of 450 nm. The cell viability (%) relative to control cells was calculated from following equation: $([Abs]_{sample} - [Abs]_{blank})/([Abs]_{control} - [Abs]_{blank}) \times 100\%$, where $[Abs]_{sample}$ and $[Abs]_{control}$ are the absorbance values of the cells with and without the treatment of nanocomplexes, respectively. The $[Abs]_{blank}$ are the absorbance of CCK-8 itself at 450 nm. All experiments were investigated in sextuplicate. Results were presented as mean ± standard deviation (SD).

Visualization of CO_2 Bubble Generation from $NaGdF_4$@$CaCO_3$-PEG nanoparticles. To observe the bubble generation characteristic of $NaGdF_4$@$CaCO_3$-PEG, the aqueous dispersion was dropped on a glass slide, followed by drying naturally. Then, PBS buffer with various pH values from 5.0 to 7.4 was dropped on the samples, and the CO_2 bubble image from $NaGdF_4$@$CaCO_3$-PEG was obtained by an optical microscope at room temperature[10,11].

***In Vitro* US Imaging at Various pH.** *In vitro* US imaging of $NaGdF_4$@$CaCO_3$-PEG was performed in phosphate buffer solutions at various pH conditions (7.4, 7.0, 6.8, and 5.0)[41]. An optically transparent phantom gel plate, which was made by embedding a 500 μL Eppendorf tube in the agarose gel (3%, w/v) and then removing the tube after the phantom gel had cooled, was used for the *in vitro* experiments. Aqueous nanoparticle solutions ($10\ mg{\cdot}mL^{-1}$) were prepared at various pH. US images were obtained using Vevo 2100 imaging system operated at 21 MHz of a static state using a contrast mode. The change of US intensity for each sample was measured up to 180 min, and the US intensity of the water as control was subtracted from the sample intensity for the normalization.

***In Vitro* MR Imaging at Various pH.** *In vitro* MR imaging of $NaGdF_4$@$CaCO_3$-PEG was performed in phosphate buffer solutions at various pH conditions (7.4, 7.0, 6.8, and 5.0) using T_1 -weighted MRI on a 0.5 T NMI20-Analyst NMR system (Niumag Corporation, Shanghai, China) to evaluate the contrast-enhancement effect[42].

Relaxivity and MRI phantom studies at 0.5T magnetic field. A series of $NaGdF_4$@$CaCO_3$-PEG nanoparticle aqueous solutions with different Gd concentrations (12.5, 10, 7.5, 5.0, 2.5, and 1.25 mM) were prepared for MRI phantom and relaxivity studies. All experiments were performed on a 0.5 T NMI20-Analyst NMR system (Niumag Corporation, Shanghai, China)[42–44]. The longitudinal relaxation times (T_1) were measured using an inversion recovery (IR) sequence. The longitudinal (r1) was determined from the slope of the plot of $1/T_1$ against the Gd concentration (mM).

***In vivo* US imaging of Xenograft Tumor.** To form a solid tumor in nude mice, the LN3 xenograft tumor was estabilished in 4-week-old male nude mice by injecting 10^6 LN3 cells into the right thigh of mice. After injection, tumor-bearing nude mice were kept for 10~14 days to achieve a tumor size around 80 mm^3. Then, 200 μL of normal saline (NS) containing $NaGdF_4$@$CaCO_3$-PEG ($2\ mg{\cdot}mL^{-1}$) was injected by an intratumoral injection. After injection, the tumor was imaged with the Vevo 2100 imaging system.

***In Vivo* MR Imaging of Xenograft Tumor.** For *in vivo* MRI measurements, LN3 tumor-bearing mice were intra-tumour injected with 200 μL of $2\ mg{\cdot}mL^{-1}$ $NaGdF_4$@$CaCO_3$-PEG. At different intervals (0–3 h), T_1-weighted MR images were observed using the rapid acquisition with relaxation enhancement sequence on 7.0 T small animal MRI scanner (Bruker Avance II 500WB spectrometer)[43]. Imaging parameters are as follows: repetition time, 2500 ms; echo time, 35 ms; rare factor, 8; field of view = $30 \times 30 mm^2$; image size, 256×256; slice thickness,0.7mm; and number of average, 2.

References

1. Jemal, A. *et al.* Global cancer statistics. *CA Cancer J Clin* **61**, 69–90 (2011).
2. Siegel, R. L. *et al.* Cancer statistics, 2016. *CA Cancer J Clin* **66**, 7–30 (2016).
3. DeSantis, C. E. *et al.* Cancer statistics for African Americans, 2016: Progress and opportunities in reducing racial disparities. *CA Cancer J Clin* **66**, 290–308 (2016).
4. Zhou, Z. *et al.* Surface and Interfacial Engineering of Iron Oxide Nanoplates for Highly Efficient Magnetic Resonance Angiography. *ACS Nano* **9**, 3012–3022 (2015).
5. Chen, N. *et al.* Folic acid-conjugated MnO nanoparticles as a T_1 contrast agent for magnetic resonance imaging of tiny brain gliomas. *ACS Appl. Mater. Interfaces* **6**, 19850–7 (2014).
6. Xing, H. *et al.* Ultrasmall $NaGdF_4$ Nanodots for Efficient MR Angiography and Atherosclerotic Plaque Imaging. *Adv. Mater.* **26**, 3867–3872 (2014).
7. Huang, G. *et al.* Highly magnetic iron carbide nanoparticles as effective T_2 contrast agents. *Nanoscale* **6**, 726–730 (2014).
8. Huang, J. *et al.* HSA coated MnO nanoparticles with prominent MRI contrast for tumor imaging. *Chem. Commun.* **46**, 6684–6686 (2010).
9. Liao, N. *et al.* Poly (dopamine) coated superparamagnetic iron oxide nanocluster for noninvasive labeling, tracking, and targeted delivery of adipose tissue-derived stem cells. *Sci. Rep* **6**, 18746 (2016).
10. Kyung, H. *et al.* pH-Controlled Gas-Generating Mineralized Nanoparticles: A Theranostic Agent for Ultrasound Imaging and Therapy of Cancers. *ACS Nano* **9**, 12 (2015).
11. Kim, M. *et al.* Nanosized Ultrasound Enhanced-Contrast Agent for *in Vivo* Tumor Imaging via Intravenous Injection. *ACS Appl. Mater. Interfaces.* **8**, 8409–18 (2016).
12. Chang, E. *et al.* F-18-FAZA PET Imaging Response Tracks the Reoxygenation of Tumors in Mice upon Treatment with the Mitochondrial Complex I Inhibitor BAY 87–2243. *Clin Cancer Res* **21**, 335–346 (2015).
13. Jiang, L. *et al.* A Radiofluorinated Divalent Cystine Knot Peptide for Tumor PET Imaging. *Mol Pharmaceut* **11**, 3885–3892 (2014).
14. Persson, M. *et al.* First F-18-labeled ligand for PET imaging of uPAR: *In vivo* studies in human prostate cancer xenografts. *Nucl. Med. Biol.* **40**, 618–624 (2013).

15. Nielsen, C. H. *et al.* PET Imaging of Tumor Neovascularization in a Transgenic Mouse Model with a Novel Cu-64-DOTA-Knottin Peptide. *Cancer Res.* **70**, 9022–9030 (2010).
16. Choi, S. H. *et al.* Large-Scale Synthesis of Bioinert Tantalum Oxide Nanoparticles for X-ray Computed Tomography Imaging and Bimodal Image-Guided Sentinel Lymph Node Mapping. *J. Am. Chem. Soc.* **133**, 5508–5515 (2011).
17. Shieh, D. B. *et al. In Vitro* and *in Vivo* Studies of FePt Nanoparticles for Dual Modal CT/MRI Molecular Imaging. *J. Am. Chem. Soc.* **132**, 13270–13278 (2010).
18. Rabin, O. *et al.* An X-ray computed tomography imaging agent based on long-circulating bismuth sulphide nanoparticles. *Nat. Mater.* **5**, 118–122 (2006).
19. Wang, L. *et al.* A Gd-doped Mg-Al-LDH/Au nanocomposite for CT/MR bimodal imagings and simultaneous drug delivery. *Biomaterials* **34**, 3390–3401 (2013).
20. Lin, L. S. *et al.* Multifunctional Fe_3O_4@Polydopamine Core-Shell Nanocomposites for Intracellular mRNA Detection and Imaging-Guided Photothermal Therapy. *ACS Nano* **8**, 3876–3883 (2014).
21. Huang, Y. *et al.* Chitosan oligosaccharide based Gd-DTPA complex as a potential bimodal magnetic resonance imaging contrast agent. *Magn. Reson. Imaging* **34**, 1–7 (2016).
22. Wang, H. *et al.* Aerosol deposition in the lungs of spontaneously breathing rats using Gd-DOTA-based contrast agents and ultra-short echo time MRI at 1.5 Tesla. *Magn. Reson. Med.* **75**, 594–605 (2016).
23. Randolph, L. M. *et al.* Polymeric Gd-DOTA amphiphiles form spherical and fibril-shaped nanoparticle MRI contrast agents. *Chem. Sci* **7**, 4230–4236 (2016).
24. Chung, M. F. *et al.* A liposomal system capable of generating CO_2 bubbles to induce transient cavitation, lysosomal rupturing, and cell necrosis. *Angew Chem-Int Edit* **51**, 10089–10093 (2012).
25. Kang, E. *et al.* Nanobubbles from Gas-Generating Polymeric Nanoparticles: Ultrasound Imaging of Living Subjects. *Angew Chem-Int Edit* **49**, 524–528 (2010).
26. Lee, S. J. *et al.* Tumor-homing photosensitizer-conjugated glycol chitosan nanoparticles for synchronous photodynamic imaging and therapy based on cellular on/off system. *Biomaterials* **32**, 4021–4029 (2011).
27. Zheng, Z. *et al.* Using "On/Off" ^{19}F NMR/Magnetic Resonance Imaging Signals to Sense Tyrosine Kinase/Phosphatase Activity *in Vitro* and in Cell Lysates. *Anal. Chem.* **88**, 3363–3368 (2016).
28. Miao, Q. *et al.* Semiconducting Oligomer Nanoparticles as an Activatable Photoacoustic Probe with Amplified Brightness for *In Vivo* Imaging of pH. *Adv. Mater.* **28**, 3662–3668 (2016).
29. Yiguang, W. *et al.* A nanoparticle-based strategy for the imaging of a broad range of tumours by nonlinear amplification of microenvironment signals. *Nat. Mater.* **13**, 204–12 (2014).
30. Mi, P. *et al.* A pH-activatable nanoparticle with signal-amplification capabilities for non-invasive imaging of tumour malignancy. *Nat. Nanotech* **11**, 724–730 (2016).
31. Liu, Z. *et al.* Iron oxide nanoparticle-containing microbubble composites as contrast agents for MR and ultrasound dual-modality imaging. *Biomaterials* **32**, 6155–63 (2011).
32. Hou, Y. *et al.* $NaGdF_4$ nanoparticle-based molecular probes for magnetic resonance imaging of intraperitoneal tumor xenografts *in vivo*. *ACS Nano* **7**, 330–338 (2012).
33. Johnson, N. J. *et al.* Size-tunable, ultrasmall $NaGdF_4$ nanoparticles: insights into their T_1 MRI contrast enhancement. *Chem. Mater.* **23**, 3714–3722 (2011).
34. Wang, F. *et al.* Preparation of core-shell $NaGdF_4$ nanoparticles doped with luminescent lanthanide ions to be used as upconversion-based probes. *Nat. Protoc.* **9**, 1634–1644 (2014).
35. Dühnen, S. *et al.* Size control of nearly monodisperse β-$NaGdF_4$ particles prepared from small α-$NaGdF_4$ nanocrystals. *Chem. Mater.* **27**, 4033–4039 (2015).
36. Jin, X. *et al.* An ultrasmall and metabolizable PEGylated $NaGdF_4$: Dy nanoprobe for high-performance T_1/T_2-weighted MR and CT multimodal imaging. *Nanoscale* **7**, 15680–15688 (2015).
37. Brugiores, P. *et al.* Randomised double blind trial of the safety and efficacy of two gadolinium complexes (Gd-DTPA and Gd-DOTA). *Neuroradiology* **36**, 27–30 (1994).
38. Johnson, N. J. J. *et al.* Size-Tunable, Ultrasmall $NaGdF_4$ Nanoparticles: Insights into Their T_1 MRI Contrast Enhancement. *Chem. Mater.* **23**, 3714–3722 (2011).
39. Zhou, C. *et al.* Aptamer $CaCO_3$ Nanostructures: A Facile, pH-Responsive, Specific Platform for Targeted Anticancer Theranostics. *Chem-Asian J* **10**, 166–171 (2015).
40. Liu, X. *et al.* SPION@$Cu_{2-x}S$ nanoclusters for highly sensitive MRI and targeted photothermal therapy of hepatocellular carcinoma. *J. Mater. Chem. B* **4**, 4119–4129 (2016).
41. Zeng, Y. *et al.* Lipid-AuNPs@PDA nanohybrid for MRI/CT imaging and photothermal therapy of hepatocellular carcinoma. *ACS Appl. Mater. Interfaces* **6**, 14266–77 (2014).
42. Zhang, D. *et al.* Lipid micelles packaged with semiconducting polymer dots as simultaneous MRI/photoacoustic imaging and photodynamic/photothermal dual-modal therapeutic agents for liver cancer. *J. Mater. Chem. B* **4**, 589–599 (2016).
43. McDonagh, B. H. *et al.* L-DOPA-Coated Manganese Oxide Nanoparticles as Dual MRI Contrast Agents and Drug-Delivery Vehicles. *Small* **12**, 301–306 (2016).
44. Frangville, C. *et al.* Hyperbranched polymer mediated size-controlled synthesis of gadolinium phosphate nanoparticles: colloidal properties and particle size-dependence on MRI relaxivity. *Nanoscale* **8**, 4252–4259 (2016).

Acknowledgements

This work is supported by the Natural Science Foundation of China (Grant No. 61575044, U1505221 and 81671813); the Science and Technology Infrastructure Construction Program of Fujian Province (Grant No. 2014Y2005); the Natural Science Foundation of Fujian Province (Grant No. 2016J0101, 2016J01329 and 2015J05175); the Scientific Foundation of Fuzhou City (Grant No. 2015-S-143-11, 2015-S-143-5).

Author Contributions

Zuwu Wei, Xiao Lin and Ming Wu designed the study, fabricated samples and wrote the manuscript. Bixing Zhao and Da Zhang provided chemical compounds and performed data analysis. Ruhui Lin, Gang Liu, and Yun Zhang helped with the MRI and US experiments. Xiaolong Liu and Jingfeng Liu designed the study, wrote the manuscript and contributed to discussion.

Additional Information

Supplementary information accompanies this paper at doi:10.1038/s41598-017-05395-w

Competing Interests: The authors declare that they have no competing interests.